Surface Microseismic Monitoring of Hydraulic Fracturing of a Shale-Gas Reservoir Using Short-Period and Broadband Seismic Sensors

by Xiangfang Zeng, Haijiang Zhang, Xin Zhang, Hua Wang, Yingsheng Zhang, and Qiang Liu

Online Material: Figure, table with double-difference event locations.

INTRODUCTION

Hydraulic fracturing has been widely applied in development of tight sand and shale gas reservoirs, in which high-pressure fluids are injected into target zones to enhance the reservoir permeability so that gas can be more efficiently recovered. The opening and growing of tensile fractures, as well as shearing slip along fractures during stimulation treatment are thought to be the major mechanisms inducing microseismic events around the treatment well (Shemeta and Anderson, 2010). Therefore, microseismic monitoring is a valuable approach to assess the fracturing process. For example, the locations of microseismic events are used to determine fracture network geometry, and their focal mechanisms are helpful for understanding how the fractures are stimulated. The information derived from microseismic monitoring is helpful for reservoir simulation and assessment (e.g., Rutledge and Phillips, 2003; Warpinski, 2009; Maxwell, 2010).

However, injecting fluids into underground formations, especially wastewater disposal into deep wells, has caused felt or damaging earthquakes with magnitudes larger than 4 in some cases (Ellsworth, 2013). The well-documented cases include Rocky Mountain Arsenal in the 1960s (Healy *et al.*, 1968), wastewater disposal in Texas (Frohlich *et al.*, 2011), Oklahoma (Holland, 2013), and Arkansas (Horton, 2012). In fact, an anomalous increase in earthquake activity has occurred in the central and eastern United States over the past few years, which is mainly due to deep injection of low-pressure wastewater into deep strata or basement formations (Ellsworth, 2013). Hydraulic fracturing using high-pressure fluids can induce a lot of earthquakes, but the vast majority have magnitudes smaller than 1 (Ellsworth, 2013). In some cases, hydraulic fracturing of shale gas can indeed cause relatively large and felt earthquakes, including an **M** 2.3 earthquake near Blackpool, United Kingdom (Green and Styles, 2012), an **M** 4.0 earthquake near Youngstown, Ohio (Kim, 2013), and an **M** 3.6 earthquake in the Horn River basin of British Columbia (BC Oil and Gas Commission, 2012).

The mechanism causing the induced seismicity is likely the well-understood process of weakening a pre-existing fault/fracture by elevating the fluid pressure (Ellsworth, 2013). This is because by injecting fluids, pore pressure in connected pores and pre-existing faults/fractures also increases. If the tectonic stress of the underground formation is close to the critical stress, it will lead to shear slip on pre-existing faults/fractures and may cause large earthquakes. For this reason, microseismic monitoring in real time is necessary for assessing the induced seismic activity so that some measures could be taken to avoid inducing large-magnitude earthquakes (Majer *et al.*, 2012).

In this study, we report results from a surface microseismic monitoring of a multiple-stage hydraulic fracturing of a shale gas reservoir along a horizontal well in early 2013. The study region is located in southwest China, where many pilot wells have been drilled to assess the shale gas development potential in China (Fig. 1). For the target hydraulic fracturing shale layer, it has a small dip angle of 7° with a thickness of ~300 m. To follow the strata trend, the horizontal well also has a dip angle of ~7°. There are 21 fracturing stages along the 1400 m-long horizontal well. The actual depth intervals of hydraulic fracturing range from ~2700 to ~3000 m (shadowed zone in Fig. 1a) from heel to toe. According to the well-logging data, limestone is the main rock type for the segment above 1300 m, whereas mudstone is the major rock type below 1300 m. The target layer is composed of shale and clay. Acoustic logging data provides a *P*-wave velocity profile between 1100 and 2400 m. The low-velocity layer corresponds to mudstone, whereas the high-velocity layer corresponds to the limestone (Fig. 1a).

Currently, for microseismic monitoring of hydraulic fracturing in industry, generally either downhole or surface monitoring is selected. For downhole microseismic monitoring, single or multiple strings of high-frequency (e.g., 15 Hz) geophones are installed in nearby well(s) (Warpinski *et al.*, 2012). For surface microseismic monitoring, densely spaced geophones consisting of thousands of high-frequency and

doi: 10.1785/0220130197

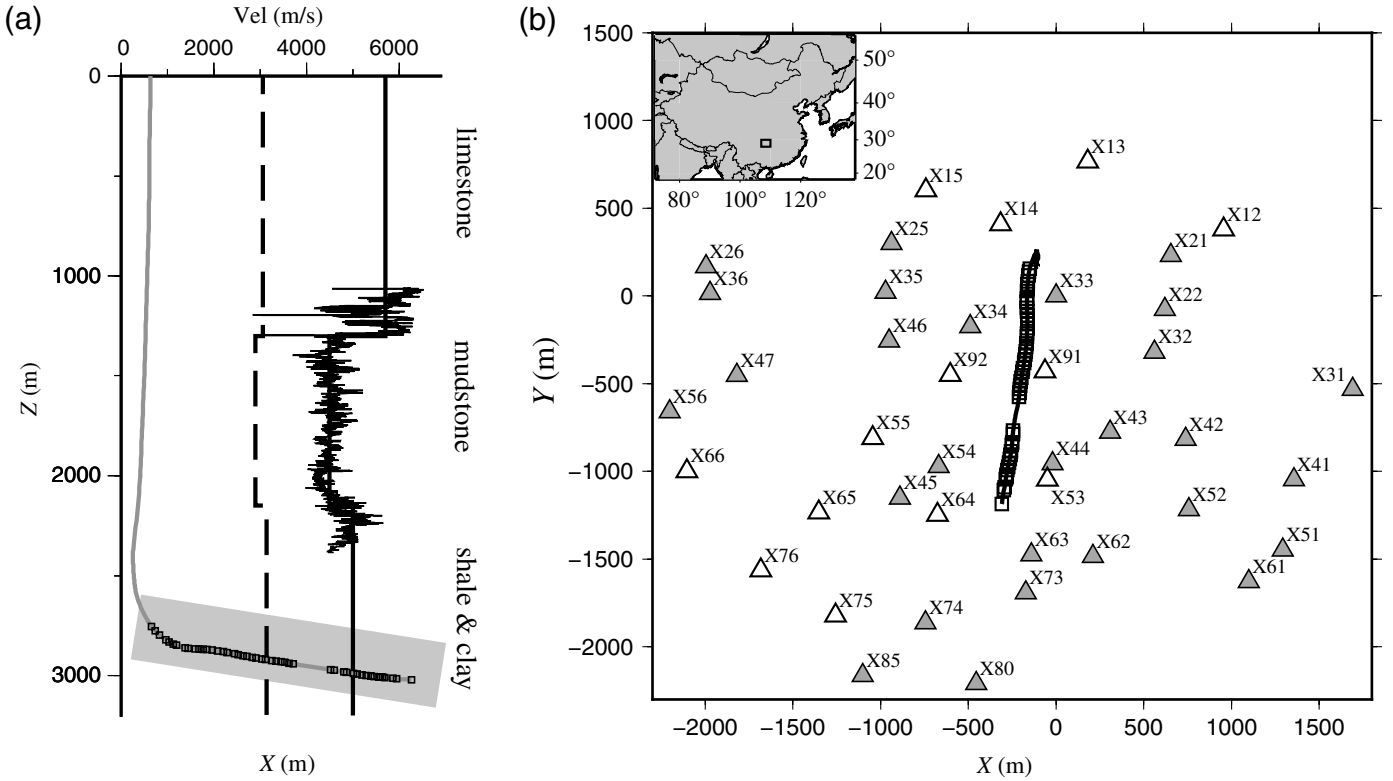

▲ **Figure 1.** (a) Layered V_P (solid line) and V_S (dashed line) models derived from sonic logging velocity curve (black) as well as the horizontal well trajectory (gray line). The gray area indicates the target shale layer. (b) Surface monitoring array (triangles) and horizontal well trajectory (black line). 27 L22E sensors are marked as filled triangles, and the other triangles are CMG-6TD sensors. Positive Y points to the north, whereas positive X points to the east. The box in the inset map marks the study area. In both (a) and (b), perforation shot locations (squares) are marked on the horizontal well trajectory.

low-sensitivity geophones are often used (Duncan and Eisner, 2010). In comparison, we used low-frequency and high-sensitivity geophones to monitor induced seismicity by hydraulic fracturing. A surface array consisting of 45 sensors was deployed around the well, with 27 L22E short-period and 18 CMG-6TD broadband seismometers (Fig. 1b). We report our process of event detection and location, and discuss event location and focal mechanism results.

EVENT DETECTION AND LOCATION

Because the dominant frequency of surface microseismic records is less than 100 Hz, the sampling rate for continuous data recording was set at 500 Hz. We continuously monitored hydraulic fracturing for about three weeks, and more than 380 GB of raw data were collected. The ratio of short-time average (STA) to the long-time average (LTA) has been widely used to detect seismic events from continuous records (Allen, 1982). Because of low signal-to-noise ratio (SNR) of the microseismic data, the conventional STA/LTA detector does not perform ideally. An extension of the STA/LTA algorithm was used to detect events in continuous records. First, a characteristic function of the raw data was constructed as follows

$$\mathrm{cf}(i) = X^2(i) - X(i+1) \times X(i-1), \tag{1}$$

which includes amplitude and its gradient. The characteristic function is more sensitive to a rapid change in waveform. Then the STA/LTA of the characteristic function was used to identify the microseismic signal. Traffic noise and missing data could also increase the STA/LTA ratios at individual stations. To suppress the erroneous detections, we used multiple traces from many stations instead of a single one. When more than six stations detected a microseismic event in a 2-s window, it was regarded as an effective detection. Time–frequency analysis of a detected event shows that P-wave energy concentrates in the frequency range of 20–60 Hz, whereas S-wave energy concentrates around 5–25 Hz (Fig. 2). To improve the SNR, continuous records were band-pass filtered between 1 and 60 Hz before event detection. Figure 2 shows an example with three effective detections. In total, more than 700 events were detected during 21 stages (Fig. 3). Although the injection rate and volume for each stage is similar, the detected event number shows some substantial variation.

Traditional arrival-time-based location methods depend on picking quality of first arrivals. However, due to strong attenuation in the near surface, SNR of data recorded by

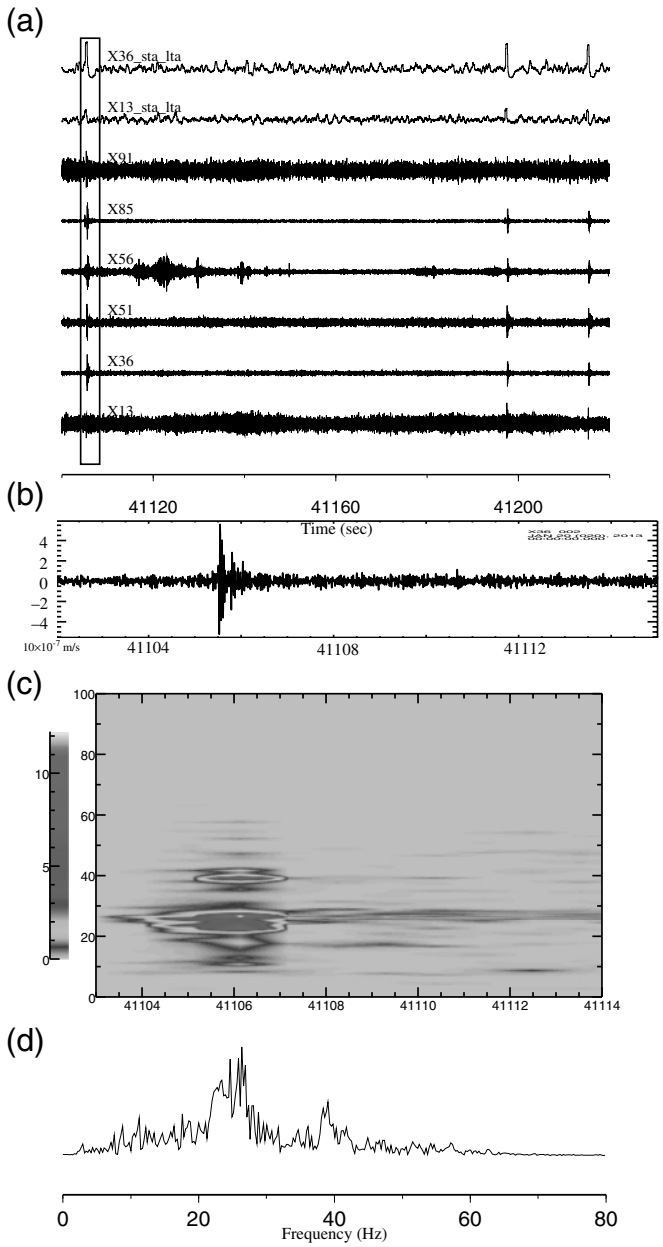

▲ **Figure 2.** (a) Traces recorded on six stations as well as the short-time average (STA)/long-time average (LTA) ratios of the corresponding characteristic functions on stations X36 and X13. (b) Trace consisting of a detected event recorded at station X36 (box in panel a). (c) Spectrogram of the waveform data in panel b. And (d), frequency spectrum of the waveform in panel b.

surface monitoring array is usually lower than that of borehole microseismic data. Low SNR of surface monitoring data generally leads to high-picking errors by an automatic picker or an analyst, thus resulting in large event location uncertainty. In some cases, it is even impossible to determine first arrivals from noisy records. In comparison, a migration-based location method does not need first arrival picking and has been successfully applied to locate glacial earthquakes, tremors, and

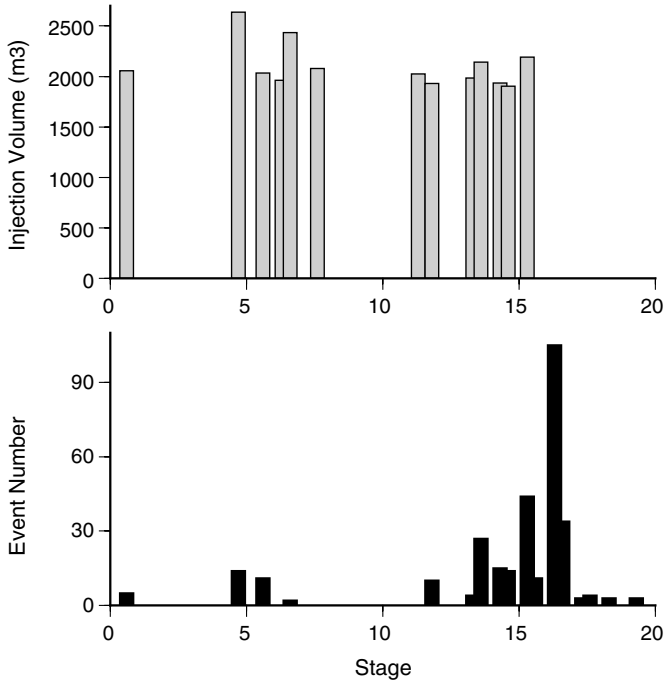

▲ **Figure 3.** The injection fluid volume (upper panel) and the detected microseismic event number (lower panel) at each stage. The fluid volume data are not available after stage 14.

noise sources (Ekström *et al.*, 2003; Kao and Shan, 2004; Zeng and Ni, 2010). For the migration-based location method, we discretized the region into 3D grid nodes. Each node can be potentially regarded as a microseismic source. The records are stacked according to travel times between stations and hypothetic source location, as well as the assumed origin time. The optimal origin time and event location are found when the stacking energy is maximum. Because of the uncertainty in the velocity model for calculating travel times and different radiation patterns at different stations, the waveforms could be out of phase, and thus direct stacking of original records could cancel each other out. Therefore, we stacked waveform envelopes instead of raw waveforms. The objective function is defined as

$$\mathrm{OBJ}(x, y, z, \tau) = \sum_{i=1}^{N} \sum_{t=-t_0}^{t_0} \{w_i[T_i(x, y, z) + \tau + t]\}. \qquad (2)$$

In the above equation, x, y, z, and τ are possible event coordinates in a 3D grid and origin time, $T_i(x, y, z)$ is the travel time from the grid point of (x, y, z) to receiver, t_0 is the half-time window size for stacking, w_i is the normalized waveform envelope at the receiver, and N is the number of receivers.

A finite-difference travel-time calculation method based on the eikonal equation was employed to calculate travel times between stations and search grid nodes (Podvin and Lecomte, 1991). During the grid-search procedure, travel time is read from the travel-time table saved on disk to speed the search

process. From the waveform of the detected event, it can be seen that the *S* wave is much stronger than the *P* wave, similar to other studies (Fig. 2). For this reason, we only stacked envelopes of the filtered seismograms in the *S*-wave windows. Because the *S* wave is stronger on horizontal components, we only stacked the north components. For stacking, a *P*-wave velocity profile between depth 1100 and 2400 m was obtained from well sonic logging (Fig. 1a). We construct a layered *S*-wave velocity model with different V_P/V_S ratios according to the rock type (Fig. 1a). The V_P/V_S ratios were chosen as 1.89 for limestone and 2.2 for shale (Castagna *et al.*, 1985).

When an event was detected, 6-s waveforms were extracted from continuous records according to the STA/LTA detected time. Then traces were normalized by the maximum absolute value to reduce the chance that the stacking result was dominated by an abnormal trace. The stacking time window length is 30 samples to reduce the uncertainty of velocity model and spike-like noise. The grid interval for the search grid is set to be 50 m in three directions. Although the V_S model used for stacking is simply derived from the sonic V_P model and the lithology-based V_P/V_S model, it is appropriate for stacking envelopes for this dataset. This can be shown by the concentrated stacking energy at the optimal event location (Fig. 4a). In addition, the theoretical arrival time calculated from the optimal location and origin time is close to the arrival of peak energy at each station (Fig. 4b).

Because event detection based on conventional STA/LTA method may give false alarms, we also rely on the waveform envelope stacking to remove unreal event locations. For the optimal origin time, the variance of the objective functions for the 3D grid nodes is used to evaluate quality of event detection. If a segment of waveform contains a real event, it is more likely that the objective functions are more focused, leading to large variance than an unreal event. Therefore, if the variance of the objective functions for the optimal origin time is large, then it is possible that the corresponding wave segment contains a real seismic event (see also fig. 2a and c in Kao and Shan, 2004). Figure 5a and b shows all 646 events with the variance greater than 1.5. For events with data having high SNRs, first arrivals were also manually picked. Starting from migration-based locations, the double-difference (DD) location method of Waldhauser and Ellsworth (2000) was employed to relocate events with manual picks to improve event locations (Fig. 5c and d). Six hundred and twenty-three events were relocated by the DD method and the root mean square travel-time residual decreased from 61.3 to 24.8 ms. In comparison with the migration-based locations (Fig. 5a and b), DD locations are less scattered in space and especially more concentrated around the horizontal well trajectory. The comparison of event locations from the migration-based location method and the arrival-based DD location method shows that, although the former is efficient and automatic to determine microseismic locations, the latter is more accurate for imaging the fracture process during hydraulic fracturing treatments. This can be more clearly seen from the comparison of the same

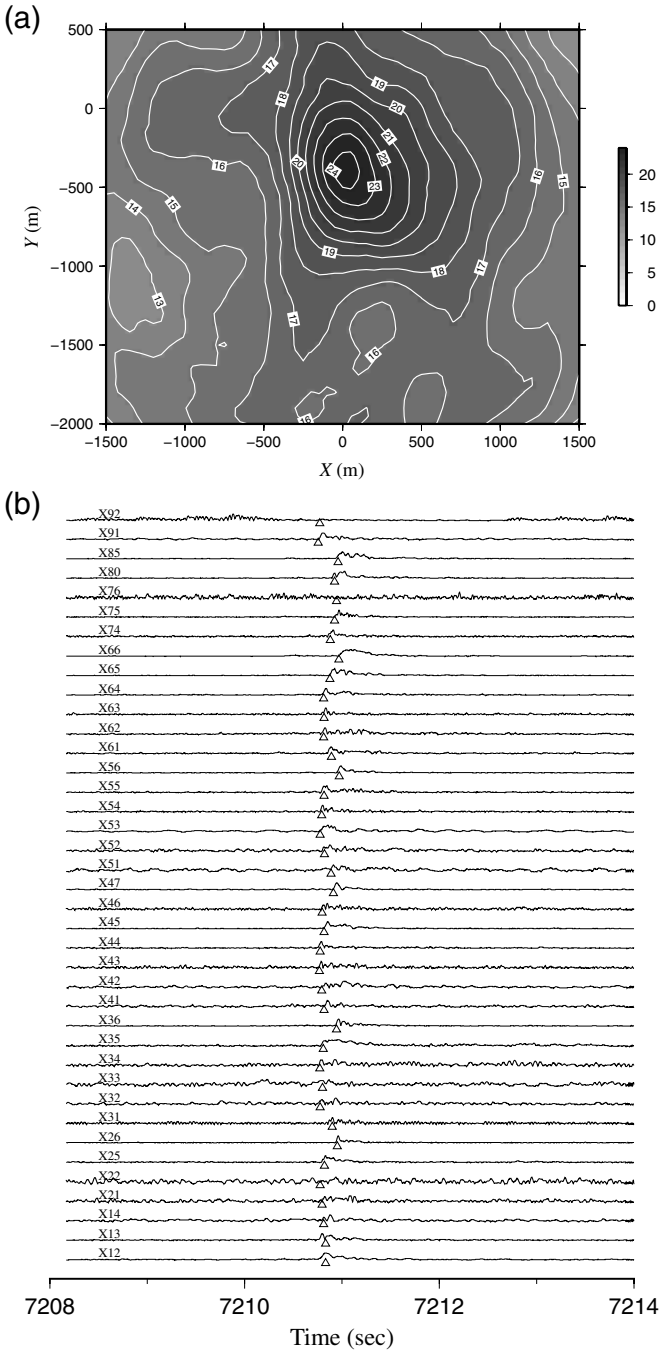

▲ **Figure 4.** (a) The contour map of the stacked energy at depth where the best event location is determined. (b) Envelopes of filtered records with theoretical arrival times (triangles) predicted from the determined event location.

set of microseismic events (Ⓔ see Fig. S1 and Table S1 in the electronic supplement to this article).

Overall, events migrated from south to north following the northward movement of hydrofracking stages (Fig. 6). The events can be categorized into two groups: group I near the wellbore and group II about 500 m east of the wellbore. Magnitudes of most events range from −2 to −1 and the two

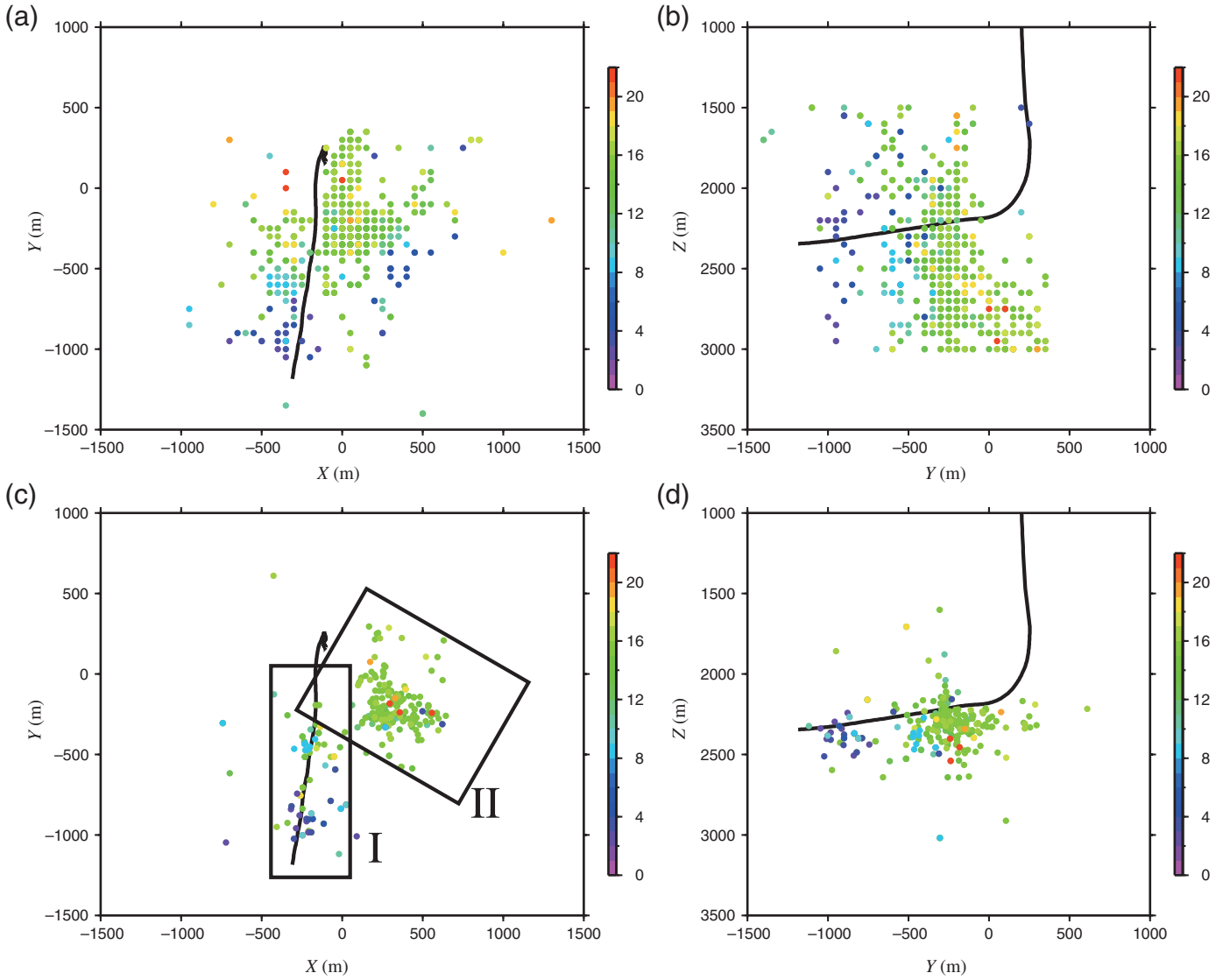

▲ **Figure 5.** (a) Map view of migration-based event locations; (b) east side view of migration-based event locations; (c) map view of DD event locations; and (d) east side view of double-difference (DD) event locations. The two boxes on panel (c) indicate event group I and II, respectively. Dot colors denote different stages.

groups have similar distributions (Fig. 7). The *b*-value for the detected microseismic events is about 1.0. During the first nine stages, events mostly occurred near the wellbore and perforation locations. However, starting from stage one, events also occur far away from the wellbore and in the group II (Fig. 6a). For the first nine stages, the group II events generally follow the northeast–southwest trend of ~60° (dashed line in Fig. 6a). At stage 10, a cluster of events is located to the east of the wellbore and is nearly perpendicular to the wellbore (dashed line in Fig. 6c). This cluster of events starts to form the majority of events of group II and until stage 16, many events repeatedly occur in the same area. After stage 16, there are fewer events detected and located. Although stimulation parameters for different stages are similar, earlier and later stages induce much fewer events than stages 10–16. It can also be seen that the group II events show two major strikes, 60° and 90° (Fig. 6a,c).

FOCAL MECHANISM ANALYSIS

The location distribution of induced events is helpful to understand stimulated reservoir volume and fracture geometry. The focal mechanisms of induced events provide additional information about fractures. Furthermore, we can use focal mechanisms to derive local stress directions. Several methods have been proposed to invert for focal mechanisms of microseismic events using first-motion polarities, relative amplitudes of first arrivals or even full waveforms (Zoback and Harjes, 1997; Duncan and Eisner, 2010; Li *et al.*, 2011). Most of small induced microseismic events could be approximated by a double-couple point source (Rutledge and Phillips, 2003) and *P* wave

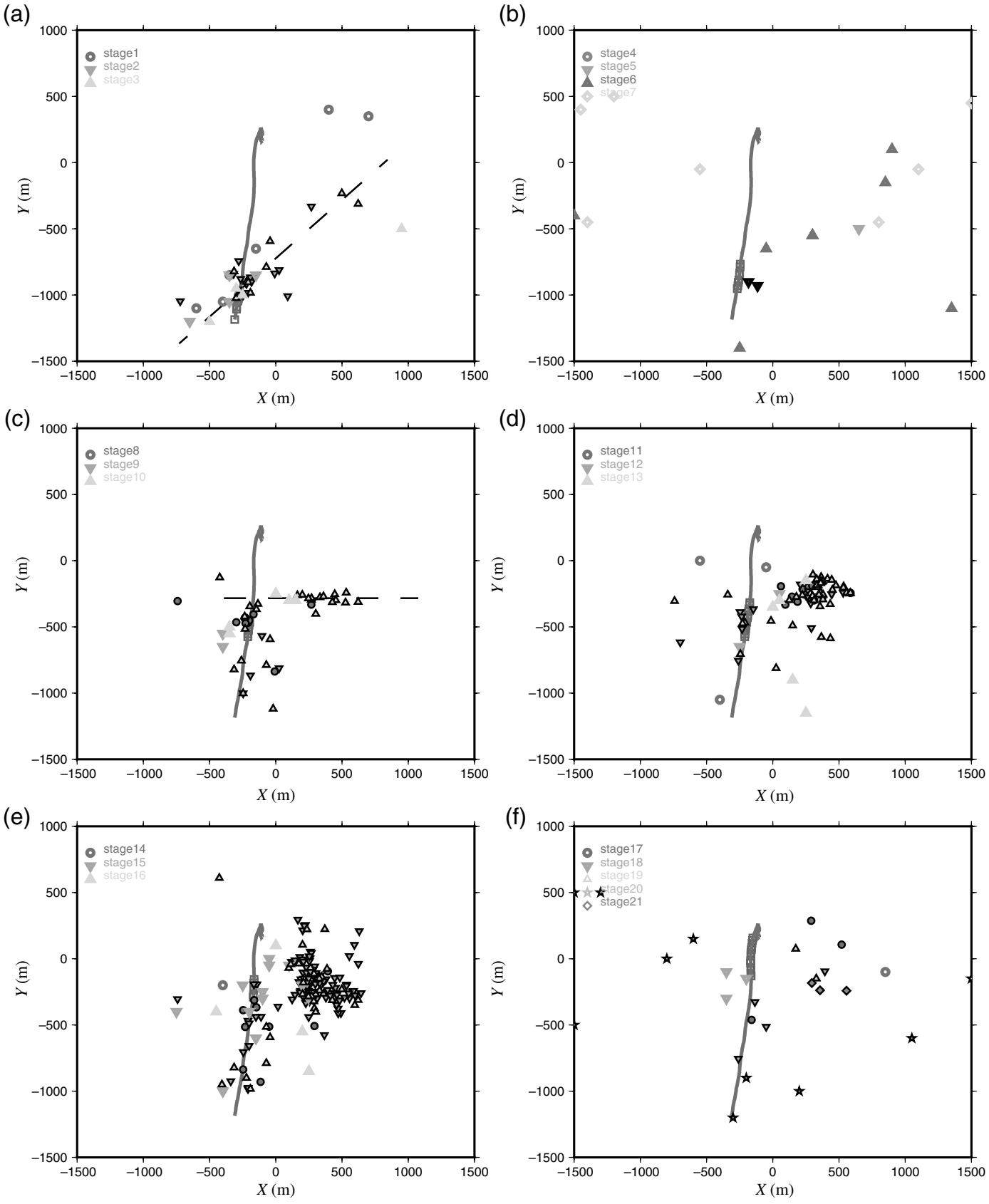

▲ **Figure 6.** Map view of event locations for different stages of hydraulic fracturing. (a) Stages 1–3; (b) stages 4–7; (c) stages 8–10; (d) stages 11–13; (e) stages 14–16; and (f) stages 17–21. Dashed lines delineate the faults/fractures illuminated by induced events.

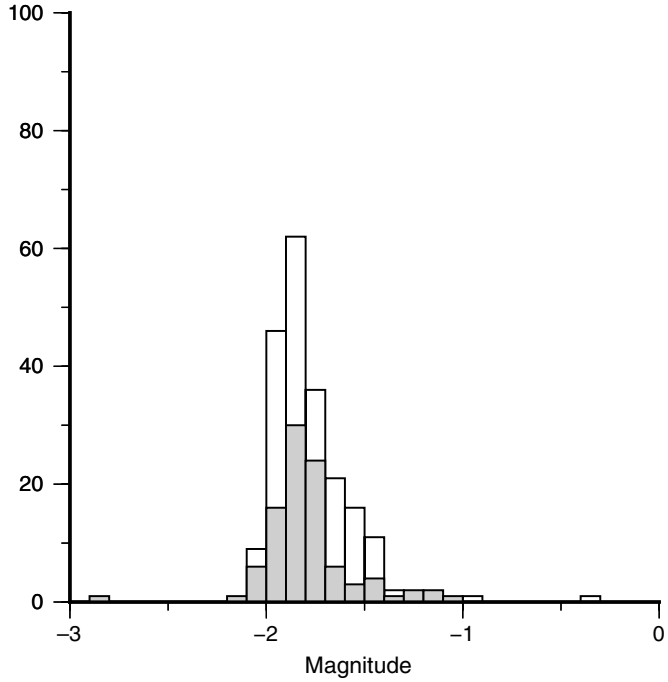

▲ **Figure 7.** Histograms of magnitudes for group I (filled) and group II (unfilled) events.

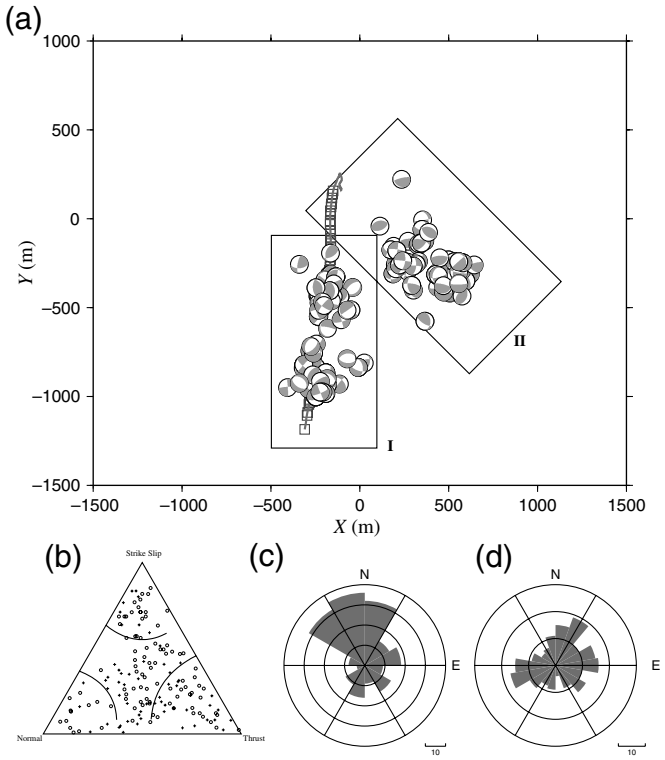

▲ **Figure 8.** (a) Map view of focal mechanisms; (b) triangle diagram of focal mechanisms, circle and cross denote events from group I and II, respectively.; (c) distribution of azimuths of *P* axes; and (d) distribution of azimuths of fault-plane strikes.

first-motion polarities have been widely used to determine the fault plane of the double-couple source. The polarity is controlled by fault plane and take-off vector. In this study, we employed the HASH method developed by Hardebeck and Shearer (2002) to determine event focal mechanisms. The take-off vector is derived from ray-path azimuth and incidence angle that are obtained from ray tracing in a layered velocity model. *P* wave first-motion polarities were manually picked on vertical records.

In total, we obtained focal mechanisms of 154 events with at least eight picks (Fig. 8a). Because of the uncertainty in the V_P model and the coverage gap of the available stations with clear first-motion polarities, it is expected that the obtained focal mechanisms also have some uncertainties. We used the misfit of the first-motion polarities to measure the focal mechanism solution quality (Hardebeck and Shearer, 2002). The average weighted misfit of first-motion polarities is less than 30.7% (Ⓔ see Table S2 in the electronic supplement). To quantitatively describe the distribution of focal mechanisms, we projected them into a triangle diagram according to the principal axes (Frohlich and Apperson, 1992). The triangle diagram is helpful to recognize event orientation clusters. For the analyzed events, the distribution of focal mechanisms is almost uniform over the focal projection. Figure 8b shows the triangle diagram for different groups of selected events, which suggests there are no significant differences between the two groups. The azimuths of compressive *P* axes are shown in a polar histogram (Fig. 8c). Most *P*-axis azimuths fall into the northwest to north-northeast directions, which is consistent with the regional-tectonic stress direction. Because of the ambiguity of the fault plane, it is difficult to determine the rupture plane. Therefore, both fault and conjugate fault are adopted in the statistics. There are two peaks (north-northeast and east-northeast) in the polar histogram (Fig. 8d). This is consistent with the previous geological survey, in which the orientation of fractures was found to range from 30° to 70° (H. Liu, personal comm., 2013). The active seismic survey also reveals an existing northeast–southwest fault in the region (H. Liu, personal comm.). Combining with the location results, it suggests that most induced events likely occurred on natural fractures.

DISCUSSION

Earthquakes release stored elastic strain energy when a shear or tensile failure occurs on a fault. The Coulomb failure condition is controlled by friction coefficient, normal stress, and pore pressure (Hubbert and Rubey, 1959). The earthquakes could be induced by increasing the shear stress, decreasing the normal stress, and/or elevating the pore pressure. When pore pressure exceeds the sum of the least principal stress and the tensile strength of the rock, it will fail in tension. Because the effective normal stress decreases as pore pressure increases, the shear failure occurs before pore pressure exceeds σ_3. In active tectonic regions, the rock is very likely critically

stressed (Zoback and Harjes, 1997), and small shear-stress/pore-pressure perturbation will cause fault slip. The earthquakes could be induced at the source of or away from stress/pore-pressure change (Ellsworth, 2013). The propagation of pore-stress perturbation is complex. In saturated rocks with low permeability, linear relaxation of pore-pressure perturbation plays a dominant role, whereas infiltration of fluid controls propagation rate (Shapiro and Dinske, 2009). Extension of fracture networks also leads to pore-pressure perturbation as well as the loss of fracturing fluid into surrounding rocks. The first mechanism shows a linear diffusion rate during fluid injection, whereas the latter mechanism shows a more complex pattern (e.g., Shapiro *et al.*, 2006). In the Perkins–Kern–Nordgren (PKN) model, both mechanisms of pore stress perturbation propagation suggest expansion of the trigger front is approximately proportional to the square root of time (Shapiro *et al.*, 2006). In comparison, for the Christianovitch–Geertsma–De Klerk-Danesh (CGDD) model, it predicts the induced events expand in proportion to 2/3 power of time (Mendelsohn, 1984), which is better than the PKN model for fitting the expansion of microseismicity with time in the Hijiori site, Japan (Sasaki, 1998). However, because of the incompleteness of the microseismic events detected in this dataset, it is difficult to show which model is more appropriate.

In this study, the group of events occurring along the wellbore seems consistent with the diffusion pattern and is near the source of stress/pore-pressure perturbation. However, during hydraulic fracturing stage 1, there are two events detected and located about 1.5 km away from the perforation spot. These two events occurred about 4.5 and 7.5 hours after the start of fluid injection, respectively. The fluid could rapidly move along a high-permeability fault, and thus the two earthquakes may be induced by the pore-pressure increase directly caused by fluid migrated from the fracturing spot. Similarly, in the case of the Horn river basin, Canada, the earthquakes are triggered along a pre-existing fault at about 200 m away from the wellbore within tens to thousands of minutes after injection (BC Oil and Gas Commission, 2012). The short time delay would require a high-permeability fault. Lockner *et al.* (2000) reported that the highest matrix permeability is up to 100 microdarcies in the damage zone of the Nojima fault of the 1995 Kobe earthquake. Indeed, the active seismic survey also reveals an existing northeast–southwest fault in the region (H. Liu, personal comm.). In this case, the transmission of pore pressure is very fast to a significant distance and is likely to cause the two earthquakes in stage 1. Alternatively, the two earthquakes could be caused by stress perturbation resulting from undrained response of fluid injection (Talwani *et al.*, 2007). If the areas with earthquakes induced are in a critical stress condition, a small stress perturbation could induce fault slip. In the following stages of 2 to 9, there are a few earthquakes induced away from the wellbore, sparsely distributed within ~1.5 km of the wellbore. These earthquakes are nominally aligned in the direction of ~60° from the north, indicating they occur along the existing faults (Fig. 6a).

For stage 10, there are more earthquakes detected and located than previous stages. These earthquakes are aligned almost perpendicular to the wellbore, and most of them are located to the northeast with respect to the perforation spot. If the wellbore is drilled along the horizontal minimal compressive stress direction, fracking-induced events would generally align perpendicular to the wellbore. However, from the focal mechanism analysis, the local horizontal maximum stress direction is approximately northwest–southeast. Therefore, these microseismic events are not directly induced by fracking, but instead most likely by reactivation along pre-existing faults/fractures. In the following stages of 11–16, there are many events repeatedly induced in the same region of ~500 to 1000 m to the east of wellbore. It is likely that the fracturing stage 10 opened a fluid conduit to the seismicity-clustering zone that is critically stressed and highly fractured. In the later stages of 11–16, the fluid can directly migrate to the clustering zone, increasing pore pressure and inducing many earthquakes.

Pre-existing faults may provide a direct conduit of fluid, which may cause a long distance trigger (Ake *et al.*, 2005; Horton, 2012). The permeability of shale is about 0.1 microdarcy, whereas the permeability of fault zone is about two orders of magnitude higher (Best and Katsube, 1995; Evans *et al.*, 1997). The breaking and crushing of grains during tectonic activities could create a fault-damage zone, which contains a mass of cracks. High-crack density increases the pore volume and fluid transport capability, for example, up to 100 microdarcies (Lockner *et al.*, 2000). The migrated fluid reduced the effective normal pressure that leads to slip of the fault. If the fault has been critically stressed and has lower friction coefficient, a small increase of pore pressure can result in a higher triggering probability, such as the case of the increased microseismic activity after stage 10. It is noted that the number of detected events shows an obvious decrease after stage 17. This could be due to less fluid leaking from the horizontal well to the pre-existing fracture/fault zone, because the leak points of pressured fluids are located to the south of the bridge plug of stage 17.

CONCLUSIONS

We used a broadband 3C seismic array installed on the surface to monitor microseismicity induced by 21 stages of hydraulic fracturing. Based on a migration-based location method and the DD location method, we obtained locations of 665 events. Our study shows that with a relatively sparse surface array it is also possible to detect and locate small magnitude events ($\mathbf{M} < -1$) induced by hydraulic fracturing. Therefore, for monitoring hydraulic fracturing in some regions with favorable surface conditions and relatively shallow reservoir zones, it is possible to use a sparse surface array.

The seismicity mainly forms two groups. Group I falls into a small volume surrounding the horizontal well and group II occurs ~500 m away from the well. We also determined focal mechanisms of 154 events with *P* wave first-motion polarities. The focal mechanism results show similar compressive stress

axis strike (northwest–north-northeast) to the regional tectonic stress direction. Both two groups show similar patterns in the triangle diagram of focal mechanisms and the strikes of fault planes are also consistent with previous geological survey. Based on locations and focal mechanisms, we conclude that the group I events are likely induced by the pore pressure increase directly caused by fluid migrated from the fracturing spot. In comparison, the group II events are likely due to reactivation of pre-existing faults/fractures by pressure perturbation from fracking, which also provide a conduit for high-pressure fluid movement.

Because the magnitude of microseismicity observed in this study is small, the risk is low. Nevertheless, it is shown that injected fluids could leak to nearby pre-existing faults and trigger earthquakes. There are several reports that injection of fluids induced felt or even damaging earthquakes on pre-existing faults (e.g., Horton, 2012; Kim, 2013). To reduce the risk of injection-induced earthquakes, better understanding of pre-existing faults, tectonic stress regime in the region, and appropriate design and management of the injection program would be necessary (Ellsworth, 2013).

ACKNOWLEDGMENTS

We are grateful to the editor Zhigang Peng, Clifford Thurber, and an anonymous reviewer for their comments that helped to improve this paper. This research is supported by Natural Science Foundation of China under Grant Number 41274055 and the Fundamental Research Funds for the Central Universities (WK2080000053). This research is also partly supported by the National Key Basic Research Program of China under Grant Number 2014CB845900.

REFERENCES

Ake, J., K. Mahrer, D. O'Connell, and L. Block (2005). Deep-injection and closely monitored induced seismicity at Paradox Valley, Colorado, *Bull. Seismol. Soc. Am.* **95,** no. 2, 664–683.

Allen, R. (1982). Automatic phase pickers: Their present use and future prospects, *Bull. Seismol. Soc. Am.* **72,** no. 6B, S225–S242.

Best, M. E., and T. J. Katsube (1995). Shale permeability and its significance in hydrocarbon exploration, *TLE* **14,** no. 3, 165–170.

British Columbia (BC) Oil, and Gas Commission (2012). *Investigation of observed seismicity in the Horn River Basin*, Victoria, British Columbia, Canada, www.bcogc.ca/node/8046/download?documentID=1270 (last accessed March 2014).

Castagna, J. P., M. L. Batzle, and R. L. Eastwood (1985). Relationships between compressional-wave and shear-wave velocities in clastic silicate rocks, *Geophysics* **50,** no. 4, 571–581.

Duncan, P., and L. Eisner (2010). Reservoir characterization using surface microseismic monitoring, *Geophysics* **75,** no. 5, 75A139–75A146.

Ekström, G., M. Nettles, and G. A. Abers (2003). Glacial earthquakes, *Science* **302,** no. 5645, 622–624.

Ellsworth, W. L. (2013). Injection-induced earthquakes, *Science* **341,** 142 pp.

Evans, J. P., C. B. Forster, and J. V. Goddard (1997). Permeability of fault-related rocks, and implications for hydraulic structure of fault zones, *J. Struct. Geol.* **19,** no. 11, 1393–1404.

Frohlich, C., and K. D. Apperson (1992). Earthquake focal mechanisms, moment tensors, and the consistency of seismic activity near plate boundaries, *Tectonics* **11,** no. 2, 279–296.

Frohlich, C., C. Hayward, B. Stump, and E. Potter (2011). The Dallas–Fort worth earthquake sequence: October 2008 through May 2009, *Bull. Seismol. Soc. Am.* **101,** no. 1, 327–340.

Green, C. A., and P. Styles (2012). Preese Hall shale gas fracturing: Review and recommendations for induced seismicity mitigation, www.gov.uk/government/uploads/system/uploads/attachment_data/file/15745/5075-preese-hall-shale-gas-fracturing-review.pdf (last accessed March 2014).

Hardebeck, J. L., and P. M. Shearer (2002). A new method for determining first-motion focal mechanisms, *Bull. Seismol. Soc. Am.* **92,** no. 6, 2264–2276.

Healy, J. H., W. W. Rubey, D. T. Griggs, and C. B. Raleigh (1968). The Denver earthquakes, *Science* **161,** no. 3848, 1301–1310.

Holland, A. A. (2013). Earthquakes triggered by hydraulic fracturing in south-central Oklahoma, *Bull. Seismol. Soc. Am.* **103,** no. 3, 1784–1792.

Horton, S. (2012). Disposal of hydrofracking waste fluid by injection into subsurface aquifers triggers earthquake swarm in central Arkansas with potential for damaging earthquake, *Seismol. Res. Lett.* **83,** no. 2, 250–260.

Hubbert, M. K., and W. W. Rubey (1959). Role of fluid pressure in mechanics of overthrust faulting I. Mechanics of fluid-filled porous solids and its application to overthrust faulting, *Geol. Soc. Am. Bull.* **70,** no. 2, 115–166.

Kao, H., and S. J. Shan (2004). The source-scanning algorithm: Mapping the distribution of seismic sources in time and space, *Geophys. J. Int.* **157,** no. 2, 589–594.

Kim, W.-Y. (2013). Induced seismicity associated with fluid injection into a deep well in Youngstown, Ohio, *J. Geophys. Res.* **118,** 3506–3518, doi: 10.1002/jgrb.50247.

Li, J., H. Zhang, H. Sadi Kuleli, and M. Nafi Toksoz (2011). Focal mechanism determination using high-frequency waveform matching and its application to small magnitude induced earthquakes, *Geophys. J. Int.* **184,** no. 3, 1261–1274.

Lockner, D., H. Naka, H. Tanaka, H. Ito, and R. Ikeda (2000). Permeability and strength of core samples from the Nojima fault of the 1995 Kobe earthquake, in H. Ito, K. Fujimoto, H. Tanaka, and D. Lockner (Editors), *Proc. of the International Workshop on the Nojima Fault Core and Borehole Data Analysis*, Tsukuba, Japan, 22–23 November 1999, *U.S. Geol. Surv. Open-File Rept. 00-129*, 147–152.

Majer, E. L., J. Nelson, A. Robertson-Tait, J. Savy, and I. Wong (2012). Protocol for addressing induced seismicity associated with enhanced geothermal systems, DOE/EE-0662, U.S. Department of Energy.

Maxwell, S. (2010). Microseismic: Growth born from success, *TLE* **29,** no. 3, 338–343.

Mendelsohn, D. A. (1984). A review of hydraulic fracture modeling. I: General concepts, 2D models, motivation for 3D modeling, *J. Energy Res. Technol.* **106,** no. 3, 369–376.

Podvin, P., and I. Lecomte (1991). Finite difference computation of traveltimes in very contrasted velocity models: A massively parallel approach and its associated tools, *Geophys. J. Int.* **105,** no. 1, 271–284.

Rutledge, J. T., and W. S. Phillips (2003). Hydraulic stimulation of natural fractures as revealed by induced microearthquakes, Carthage Cotton Valley gas field, east Texas, *Geophysics* **68,** no. 2, 441–452.

Sasaki, S. (1998). Characteristics of microseismic events induced during hydraulic fracturing experiments at the Hijiori hot dry rock geothermal energy site, Yamagata, Japan, *Tectonophysics* **289,** no. 1, 171–188.

Shapiro, S. A., and C. Dinske (2009). Fluid-induced seismicity: Pressure diffusion and hydraulic fracturing, *Geophys. Prospect.* **57,** no. 2, 301–310, doi: 10.1111/j.1365-2478.2008.00770.x.

Shapiro, S. A., C. Dinske, and E. Rothert (2006). Hydraulic-fracturing controlled dynamics of microseismic clouds, *Geophys. Res. Lett.* **33,** no. 14, L14312, doi: 10.1029/2006GL026365.

Shemeta, J., and P. Anderson (2010). It's a matter of size: Magnitude and moment estimates for microseismic data, *TLE* **29,** no. 3, 296–302.

Talwani, P., L. Chen, and K. Gahalaut (2007). Seismogenic permeability, K_s, *J. Geophys. Res.* **112,** no. B07309, doi: 10.1029/2006JB004665.
Waldhauser, F., and W. L. Ellsworth (2000). A double-difference earthquake location algorithm: Method and application to the northern Hayward fault, California, *Bull. Seismol. Soc. Am.* **90,** no. 6, 1353–1368.
Warpinski, N. (2009). Microseismic monitoring: Inside and out, *J. Petrol. Technol.* **61,** no. 11, 80–85.
Warpinski, N. R., J. Du, and U. Zimmer (2012). Measurements of hydraulic-fracture-induced seismicity in gas shales, *SPE Prod. Oper.* **27,** no. (3), 240–252.
Zeng, X., and S. Ni (2010). A persistent localized microseismic source near the Kyushu Island, Japan, *Geophys. Res. Lett.* **37,** no. 24, L24307, doi: 10.1029/2010GL045774.
Zoback, M. D., and H. P. Harjes (1997). Injection-induced earthquakes and crustal stress at 9 km depth at the KTB deep drilling site, Germany, *J. Geophys. Res.* **102,** no. B8, 18477–18491.

Xiangfang Zeng[1]
Haijiang Zhang[2]
Xin Zhang[2]
Hua Wang[3]

Wantai-BMT Microseismic Lab of
School of Earth and Space Sciences
University of Science and Technology of China
Hefei 230026, China
zhang11@ustc.edu.cn

Yingsheng Zhang
Qiang Liu
Beijing Miseis Technologies
Beijing 100096, China

[1] CAS Key Laboratory of Computational Geodynamics, University of Chinese Academy of Sciences, Beijing 100049, China.
[2] Laboratory of Seismology and Earth's Interior, University of Science and Technology of China, Hefei 230026, China.
[3] College of Geophysics and Information Engineering, Petroleum University, Beijing 102249, China.